nature photonics

SUPPLEMENTARY INFORMATION

DOI: 10.1038/NPHOTON.2013.174

Supplementary Information

Tenfold reduction of Brownian noise in high-reflectivity optical coatings

Garrett D. Cole[1,2,*], Wei Zhang[3,*], Michael J. Martin[3], Jun Ye[3], and Markus Aspelmeyer[1]

[1] *Vienna Center for Quantum Science and Technology (VCQ), Faculty of Physics, University of Vienna, A-1090 Vienna, Austria*

[2] *Crystalline Mirror Solutions GmbH, A-1090 Vienna, Austria*

[3] *JILA, National Institute of Standards and Technology and University of Colorado, Boulder, Colorado 80309-0440, USA*

S1. Finesse Estimation

Calculation of the cavity finesse requires quantification of the various loss mechanisms of the end mirrors. As our crystalline coatings are constructed from identical multilayers (sourced from neighbouring locations on the same epitaxial wafer) we assume that the individual coatings have a matched reflectance. Below we provide a description of the steps taken in order to characterize the transmission, scatter, and absorption loss of the mirrors. In each case measurements are performed both on the original growth wafer and after bonding in order to investigate any potential changes in the optical properties following the substrate-transfer process.

---

[*] These authors contributed equally to this work.

DOI: 10.1038/NPHOTON.2013.174

In order to determine the mirror transmission, the reflectance spectrum of the DBR is recorded via spectrophotometry, as shown in Fig. 1c. Fitting of the mirror stopband with a transmission matrix model, using x-ray diffraction derived composition and thickness values as a baseline, it is possible to extract the individual layer thicknesses for the high and low index components of the multilayer. Fortunately, given the long history of application in optoelectronics (e.g. Ref. 1), the refractive index and dispersion characteristics are very well known for the AlGaAs materials system. This fitting technique is exquisitely sensitive to variations in thickness, with changes on the order of 1 nm for individual layer thicknesses resulting in shifts of the center wavelength of the high-reflectivity stopband by nearly 10 nm. The fitted transmission matrix model is then used for an accurate estimate of the transmission loss of the mirror. For the 40.5 period DBR employed here, the extracted transmission is 4 ppm. Independent measurement of the transmission of a post-bonded crystalline coating (on a fused silica substrate) yields 3.8 ppm, verifying the accuracy of this approach. One current limitation in our process is the lack of an *in situ* optical monitor in the MBE system. Thus, it is difficult to reliably realize a desired transmission value. With this in mind, early mirrors were designed with minimal transmittance in order to avoid the possibility of insufficient finesse.

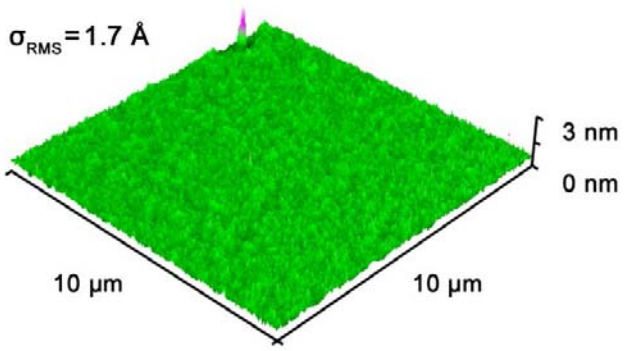

Figure S1: Post-bond AFM characterization of the AlGaAs DBR surface quality. The measured RMS roughness of 1.7 Å (determined by averaging line scans over a 10 µm × 10 µm area) leads to a calculated scatter loss of 4 ppm for the crystalline coating. The defect in the top corner of the scanned area is excluded from the roughness calculation, but is included here to show the potential for imperfections in the multilayer.

Atomic force microscopy (AFM) is used to characterize the surface roughness, and ultimately the scatter loss, of both the pre- and post-bonded mirror structure. For our MBE-grown AlGaAs DBR, we record a root mean square (RMS) roughness value of 1.7 Å over a 10 μm × 10 μm scan area, as shown in Figure S1. Note that this measurement was made following the transfer process and remains unchanged when compared with the on-wafer surface quality. Assuming normal-incidence illumination of a surface characterized by an RMS roughness σ, the scatter-limited reflectance is determined from the expression derived by Davies[2] $R_s = e^{\frac{-(4\pi\sigma)^2}{\lambda^2}}$. In the long wavelength (for surface features much smaller than the wavelength λ) and high reflectivity limit, this expression yields a fairly accurate estimate of the reflectance and thus the corresponding scatter loss value (1-R_s) [3]. Using our measured AFM data and a wavelength of 1064 nm, we calculate a scatter loss of 4 ppm for the AlGaAs DBR. The validity of the further simplification of taking into account only the *surface* roughness of the multilayer is ultimately verified by the excellent agreement between our theoretical and measured finesse values (1.53×10^5 versus $1.5(1)\times10^5$ respectively).

The final component necessary to estimate the cavity finesse is the optical absorption. This parameter is probed directly via photothermal common path interferometry (PCI) [4]. Absorption data extracted by PCI reveal typical loss levels of ~10 ppm (unchanged for both pre- and post-bond conditions) for our MBE-grown AlGaAs mirrors at 1064 nm[5], with the current best measurement below 5 ppm. For the sample used in the study, the average absorption value was slightly higher at 12.5±1.19 ppm (with a somewhat large sample-to-sample variation). A series of three linear scans (11.1±0.08 ppm, 12.9 ±0.12 ppm, and 13.5±1.18 ppm) were averaged for this measurement; a typical example is presented in Figure S2.

We are currently operating under the assumption that this property is dominated by free-carrier absorption (FCA). In contrast, calculations of the two-photon absorption at 1064 nm yields single digit or sub-ppm absorption values for realistic intra-cavity powers[6]. Unfortunately,

DOI: 10.1038/NPHOTON.2013.174

with these thin films and at these low carrier concentrations, direct characterization of the carrier type and concentration via Hall measurement is extremely difficult. Assuming that the corresponding absorption coefficient of 0.38 cm^{-1} (calculated from the 12.5 ppm absorption value over a round-trip penetration depth of 163 nm) is dominated by a *p*-type impurity background and extrapolating from the data presented in Kudman and Seidl[7], the estimated carrier concentration for this structure is 2.5×10^{16} cm^3.

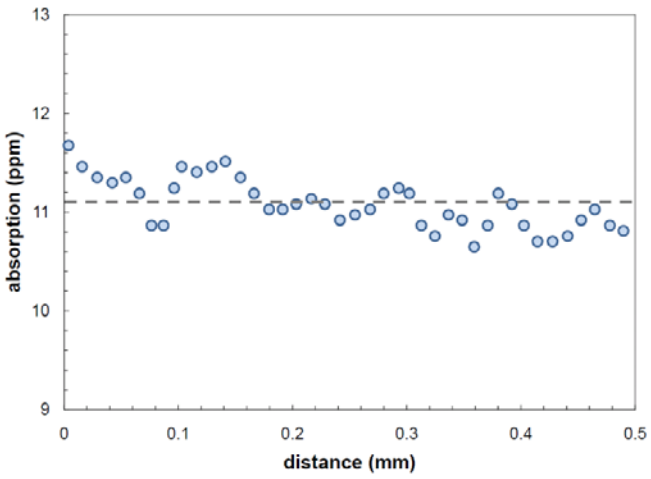

Figure S2: Typical PCI line-scan for characterizing the optical absorption of the bonded crystalline coating. The average absorption in this example is 11.1±0.08 ppm at 1064 nm. Averaging of three line scans yields a mean absorption value of 12.5 ppm for the 40.5-period AlGaAs DBR.

With FCA in the high index layers being the ultimate limit, it should be possible to generate high reflectivity AlGaAs-based mirrors out to approximately 3 μm[8], while moving to wavelengths shorter than the current implementation at 1064 nm will necessitate a significant increase in the average Al content in order to stave off interband absorption. Previous work with visible VCSELs has demonstrated high quality AlGaAs DBRs with center wavelengths as short as 650 nm[9], though further research will be necessary to quantify the minimum achievable absorption levels in this wavelength window. Note that operation at 698 nm will be directly relevant for Sr optical atomic clock applications.

S2. Birefringence Calculations

As discussed in the manuscript, the mode structure of the fixed spacer cavity constructed with the AlGaAs-based crystalline coatings reveals two orthogonal polarization eigenmodes with a splitting of 4(0.4) MHz. Interestingly, the refractive index of unstrained (100)-oriented ternary $Al_xGa_{1-x}As$ alloys is in-plane isotropic, meaning that, from the point of view of a reflecting surface-normal beam, there is no radial variation in index. Thus, for an ideal cavity constructed from perfect crystalline coatings, there will be no birefringence. However, anisotropy can easily be introduced through the application of strain in the system, leading to a corresponding directional dependence on index via the elasto-optic effect. For the bonded mirrors there are two possible paths for strain being imparted on the mirror: 1) bending-induced strain generated when fabricating the curved mirror and 2) internal strains resulting from the epitaxial growth process.

Path 1 requires a finite element model in order to calculate the imparted strain on the deformed mirror. In this case the mirror disc (8 mm in diameter by 6.83 μm in thickness) is forced into a prescribed displacement described by $x^2 + y^2 + (z - 0.999992)^2 = 1\ \mathrm{m}^2$ (with x and y lying within the plane of the originally flat mirror and z being the vertical direction normal to the DBR surface), forcing the mirror to conform to a sphere of 1-m radius with a maximum deflection of 8 μm at the mirror center. Incorporating the average density and elastic constants of the single-crystal multilayer (ρ=4551 kg/m^3; c_{11}=119.94, c_{12}=55.38, and c_{44}=59.15 GPa), the mean in-plane stress, $\frac{1}{2}(\sigma_{xx} + \sigma_{yy})$, is found to be approximately 500 kPa (compressive) on the front surface of the mirror and is essentially uniform across the mirror face given the constant radius of curvature of the deformed multilayer. Note that this is an extremely small stress value compared with the hundreds of MPa or even GPa levels of internal stress found in typical ion

DOI: 10.1038/NPHOTON.2013.174

beam sputtered films. There are two take-home messages from this exercise: i) for a bonded mirror with a 1-m ROC, we are imparting very little strain in the multilayer, so there is no fear of damaging the structure, and ii) given the miniscule stress (and corresponding strain value), this is likely not the cause of the birefringence.

For a quick estimate, path 2 (growth-induced strain) can be calculated using simple analytical expressions. As we employ a well-known epitaxial materials system, it is quite easy to extract the internal strain arising from slight differences in the inter-atomic spacing between the constituent components of the multilayer, or in other words, due to the differential thermal contraction of the layers upon cooling, from the growth, to room temperature, T. Notably, for $Al_xGa_{1-x}As$ compounds, the lattice parameter is nearly exactly matched for typical deposition temperatures[10]. At room temperature, the high index film, consisting of binary GaAs, is characterized by a lattice parameter, a, of 5.6533 Å, while for $Al_{0.92}Ga_{0.08}As$ this value is 5.6605 Å. This slight difference in lattice constant leads to a mismatch strain, e_m, of 1.27×10^{-3} when cooling from ~900 K to 300 K, in general agreement with previous investigations showing CTE-driven mismatch values slightly over 1 millistrain for films of similar average aluminum content[11-13]. Assuming an average isotropic Young's modulus, E, of 100 GPa for the multilayer, the resulting mismatch-driven stress, X, is then 127 MPa (simply determined from $\sigma = eE$). Obviously, this value is significantly larger (>250×) than the bending-induced stress described above and is thus the more likely source of the observed polarization splitting.

Realizing a first-order estimate of the index change with this internal strain is fairly straightforward. The principal axes of birefringence in zincblende crystals under a uniform applied strain is the [110] family of directions; in that case the resulting index difference[1]

between the parallel and perpendicular axes is described by $\Delta n = \frac{1}{2}\sqrt[-1]{\varepsilon}\alpha_{pe}X$, where ε is the real part of the dielectric constant at optical frequencies, α_{pe} is the photoelastic coefficient, and X is the internal stress in the multilayer. Plugging in the average photoelastic coefficient of 5×10^{-11} Pa^{-1} and high frequency dielectric constant of 12, both values from Ref. [13], along with the previously calculated stress value (127 MPa), yields an index difference of roughly 1×10^{-3}.

Calculation of the frequency splitting requires knowledge of the optical path length including the vacuum cavity (L_{cav} = 35 mm), plus the additional field penetration depth into the mirrors[15]. For the 40.5-period AlGaAs DBR employed in this experiment, the penetration depth, L_{pen}, at 1064 nm is calculated to be 163 nm. The change in length from the strain-driven index perturbation, δ, is determined to be $2L_{pen}\Delta n$ = 3.3 Å. Converting this physical length to a frequency difference, Δf, results in a maximum polarization splitting of 5.3 MHz for a center wavelength of 1064 nm (f_0=2.82×10^{14} Hz) using $\Delta f \approx f_0 \frac{2\delta}{L_{cav}}$. This value compares well with our measurement of 4(0.4) MHz for a randomly oriented pair of crystalline coatings. For future runs, the mirror discs should include features indicating the crystallographic orientation of the coatings in order to maintain the desired alignment.

DOI: 10.1038/NPHOTON.2013.174

S3. Thermal Noise Measurement and Calculations

The Methods Summary provides basic information as required for the calculation of the thermal noise results presented in the Letter. Below we present a detailed discussion of the thermal noise model and introduce the relevant parameters used in the present work.

Thermal noise theory: The single-sideband power spectral density of the thermal noise displacement (G_{total}), consisting of Brownian motion of the spacer (G_{spacer}), substrate (G_{sub}), and coating (G_c), substrate thermoelastic noise (G_{TE}) and coating thermo-optic noise (G_{TO}), is described by the following[5,16-23] (symbols and corresponding values defined in Table 1):

$$\begin{aligned} G_{total}(f) &= G_{spacer}(f)+G_{sub}(f)+G_c(f)+G_{TE}(f)+G_{TO}(f) \\ &= \frac{2k_BT}{\pi^2 f}\frac{L}{(R^2-r^2)Y_{spacer}}\phi_{spacer}+\frac{4k_BT}{\pi^{3/2}f}\frac{1-\sigma_{sub}^2}{w_mY_{sub}}\phi_{sub} \\ &+\frac{4k_BT}{\pi^2 f}\frac{1-\sigma_{sub}^2}{w_mY_{sub}}\frac{D}{w_m}\frac{\phi_c}{Y_{sub}Y_c(1-\sigma_c^2)(1-\sigma_{sub}^2)}\left[Y_c^2(1+\sigma_{sub})^2(1-2\sigma_{sub})^2+Y_{sub}^2(1+\sigma_c)^2(1-2\sigma_c)\right] \\ &+G_{TE}(f)+G_{TO}(f) \end{aligned} \tag{1}$$

Here,

$$G_{TE}(f)=\frac{8}{\sqrt{\pi}}(1+\sigma_{sub})^2\alpha_{sub}^2\frac{k_BT^2w_m}{\kappa_{sub}}\times\int_0^{+\infty}du\int_{-\infty}^{+\infty}dv\sqrt{2/\pi^3}u^3e^{-u^2/2}/\{(u^2+v^2)[(u^2+v^2)^2+\Omega_{TE}^2(f)]\}$$

$$\Omega_{TE}(f)=w_m^2C_{sub}\pi f/\kappa_{sub}$$

and

$$G_{TO}(f)=\frac{4k_BT^2}{\pi^{3/2}w_m^2\sqrt{f\kappa_{sub}C_{sub}}}\Gamma_{TO}(f)(\bar{\alpha}_cD-\bar{\beta}_c\lambda-\bar{\alpha}_{sub}DC_c/C_{sub})^2 \qquad (\ w_m^2C_{sub}\pi f/\kappa_{sub}>>1\ )$$

$$G_{TO}(f)=\frac{4k_BT^2}{\sqrt{\pi}w_m\kappa_{sub}}(\bar{\alpha}_cD-\bar{\beta}_c\lambda-\bar{\alpha}_{sub}DC_c/C_{sub})^2 \qquad (w_m^2C_{sub}\pi f/\kappa_{sub}<<1),$$

where $\Gamma_{TO}(f)$ is the thickness correction factor of the coating layer[5,22]. The expression of G_{TO} at high and low frequencies are based on the treatments shown in Ref. 21 and 22.

Table 1. Symbols and parameters used in the thermal noise calculations. Here, "*spacer*" refers to the zerodur cavity spacer, the "*sub*" index is for the fused silica substrates, and "*c*" represents the AlGaAs crystalline coating.

Parameter	Description	Value
λ	Wavelength	1.064 μm
f	Fourier frequency	
L	Cavity length	35 mm
R	Spacer radius	15 mm
r	Central bore radius	5 mm
$Y_{spacer/sub/c}$	Young's modulus spacer/substrate/coating	91 / 72 / 100 GPa
$\phi_{spacer/sub/c}$	Loss angle spacer/substrate/coating	3×10^{-4}/ 1×10^{-6}/ 2.5×10^{-5}
$\sigma_{sub/c}$	Poisson ratio substrate/coating	0.17/0.32
w_m	Beam radius	250 μm
D	Coating thickness	6.83 μm
T	Temperature	300 K
k_B	Boltzmann's constant	1.38×10^{-23} J/K
$C_{sub/c}$	Heat capacity per volume substrate/coating	1.71×10^{6} / 1.64×10^{6} J/ Km^3
$\kappa_{sub/c}$	Thermal conductivity substrate/coating	1.38 / 62.9 W/Km
$\overline{\alpha}_{sub/c}$	Effective coefficient of thermal expansion substrate/coating	~~1.2×10^{-6}~~ / 1.68×10^{-5} 1/K
$\overline{\beta}_c$	Effective thermorefractive coefficient (coating)	5×10^{-5}

The corresponding frequency noise G_υ is

$$G_\nu(f) = G_x(f)\times\frac{\nu^2}{L^2}, \tag{2}$$

Where G_x is the thermal displacement noise corresponding to each contribution shown in Eq. 1 and υ is the optical frequency. Eqs. 1 and 2 allow us to determine the theoretical thermal-noise-limited frequency noise, which is shown as the violet line in Figure 4b.

For the type of frequency counter employed in this measurement, the theoretical thermal noise-limited fractional frequency stability, σ_y, is equal to[24]

$$\sigma_y^2(\tau) = \int_0^\infty \frac{G_\nu(f)}{\nu^2}\times 32\frac{(\sin(\pi f\tau/2))^4\times|\sin(\pi f\tau)|^2}{(\pi f\tau)^4}df\,. \tag{3}$$

DOI: 10.1038/NPHOTON.2013.174

Employing Eqs. 1 to 3 and the parameters of the Fabry-Pérot cavity listed in Table 1, the thermal noise limited values of G_x and σ_y (at 1 Hz and 1 s, respectively) can be calculated. These results are summarized in Table 2. To facilitate measurement of the contribution from the mirror coatings, a relatively short spacer length of 35 mm is chosen for the experiment.

Table 2. Theoretical calculation of thermal noise in the crystalline-coating cavity. Displacement values G_x are shown at 1 Hz and the Allan deviation σ_y at 1 s. Assumed loss angles of zerodur, fused silica, and the crystalline coating are 3×10^{-4}, 1×10^{-6}, and 2.5×10^{-5}, respectively.

Noise type		G_x ($\times10^{-34}$) m^2/Hz	σ_y ($\times 10^{-16}$)	Contribution to total $(\sigma_y)^2$		Total σ_y ($\times 10^{-15}$)
Brownian motion	Spacer	4.8	8.4	56 %	86%	1.1
	Substrate	1.6	4.9	19%		
	Coating	0.9	3.6	11%		
Substrate thermoelastic		1.7	4.1	13%		
Coating thermo-optic		0.2	1.1	1%		

The results in Table 2 clearly demonstrate that Brownian noise makes the main contribution to the predicted total thermal noise. The fractional frequency stability as predicted by the total theoretical thermal noise is 1.1×10^{-15} at 1 s, where the contribution from the crystalline coating is approximately 11% when assuming a loss angle of 2.5×10^{-5} as measured in free-standing resonators. This can be compared with conventional dielectric end mirrors where 70% of the loss is attributed to the amorphous SiO_2/Ta_2O_5 layers. Though admittedly small in terms of the overall fractional contribution, the coating Brownian noise contribution is large enough to be isolated from other noise sources, allowing us to extract the coating loss angle by measuring the stability of the 1064 nm cavity-stabilized laser. The crystalline coating loss angle is evaluated to be $0(4)\times10^{-5}$,corresponding to the measured σ_y of f_{b1064} at 1 s averaging time, using a loss angle of 3×10^{-4} for the zerodur spacer and 1×10^{-6} for the fused silica substrate[16]. The

error in the AlGaAs loss angle is based on a 10% error in the measured σ_y as well as a 20% uncertainty in the loss angles of the cavity components, including the zerodur spacer and fused silica substrates*.

Details on the Yb frequency comb: The carrier-envelop-offset, f_{ceo}, is generated by a *f-2f* self-referencing interferometer and stabilized on a RF reference via feedback to an AOM, acting as the fast actuator, and the temperature of a fiber Bragg grating as the slow actuator[25]. The bandwidth of the f_{ceo} servo loop is approximately 160 kHz. To phase lock the Yb comb to the 698 nm clock laser, the optical heterodyne beat, f_{b698}, between a comb tooth and the clock laser is stabilized using the intracavity EOM as a fast actuator and a cavity end-mirror mounted on a piezoelectric transducer (PZT), as well as a PZT-based fiber stretcher, as slow actuators. The bandwidth of the f_{b698} servo loop is about 150 kHz.

Stabilization of the 1064 nm laser: The cavity-stabilized laser at 1064 nm is a continuous wave all solid-state, diode-pumped non-planar ring oscillator (NPRO). Since the free-running laser linewidth is only a few kHz—much narrower than the Fabry-Pérot cavity linewidth—an additional pre-stabilization stage can be avoided.

The reference cavity and supporting structure are installed in a vacuum chamber with a residual pressure of 10^{-6} torr (1 torr = 133.3 Pa) provided by an ion pump (2 liter/s pumping speed). The temperature of the vacuum chamber is 300 K with variations smaller than 1 mK over a 24 hour period. The vacuum chamber and optical components for the RF sideband lock are

* If we perform an identical calculation with a fused silica loss angle of 10^{-7}, we obtain a loss angle of $4(4)\times10^{-5}$ for the substrate-transferred AlGaAs multilayer.

DOI: 10.1038/NPHOTON.2013.174

located on a passive vibration isolation platform (Minus K, 0.5-1 Hz resonance frequency). The laser output is divided into two components: the majority of the optical power is sent to the Yb comb system for intercomparison, while the remaining 10% of the output power is fiber-coupled to the platform for RF sideband locking to the reference cavity. A fiber-based EOM provides phase modulation for locking, with its residual amplitude modulation (RAM) actively stabilized to well below the predicted thermal noise floor[26-28]. The single frequency laser is stabilized to the Fabry-Pérot cavity via feedback to the laser cavity PZT with a servo bandwidth of approximately 40 kHz.

S4. Reduction of excess thermo-optic with an optimized AlGaAs coating

As discussed in the Article, our AlGaAs multilayer displays significant thermo-optic noise at frequencies exceeding 10 Hz. This excess noise arises from the relatively large values of the effective thermorefractive and thermal expansion coefficients for this design and materials system, as can be seen in Table 1. However, it is important to note that this limitation should be fairly straightforward to overcome. According to the thermo-optic noise expression given in Eq. 1 (from Refs. [5] and [22]), the addition of a half-wavelength cap to our current multilayer design can reduce this noise contribution by a factor of roughly 2, as shown in Figure S3. Consequently, employing such an optimized design, the coating Brownian noise is then predicted to dominate the total coating thermal noise. Compared with the theoretical thermal noise of a traditional SiO_2/Ta_2O_5 multilayer as shown in Figure 4c, the corresponding improvement of the AlGaAs multilayer with the additional cap layer will be at least a factor of 10 over the entire range from 1 Hz to 100 Hz. Future implementations of AlGaAs-based crystalline coatings will

thus incorporate this additional material in order to significantly reduce the thermo-optic noise contribution.

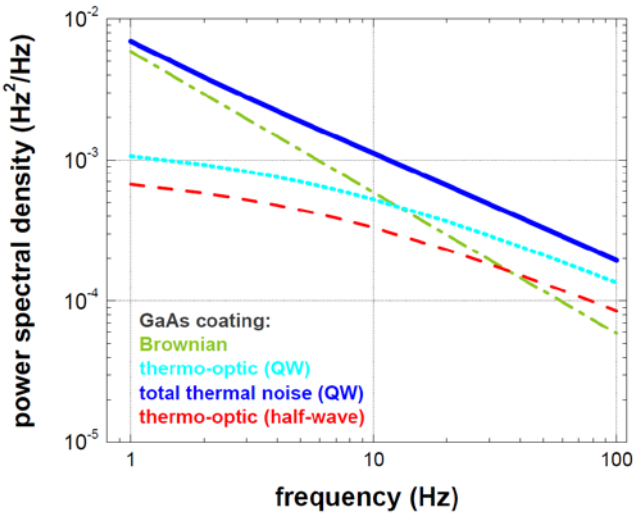

Figure S3: Comparison of the thermal noise performance of substrate-transferred AlGaAs coatings with and without a half-wavelength cap. The green dot-dashed line is the AlGaAs Brownian noise, the cyan dotted line is the thermo-optic noise for an AlGaAs multilayer using a standard quarter-wave (QW) design, while the blue solid line is the total thermal noise for such a structure. When a half-wavelength cap is added to the QW AlGaAs multilayer, the thermo-optic noise is reduced, particularly at low frequencies, as indicated by the red dashed line. In this case the total thermal noise for the optimized structure would be limited primarily by the Brownian noise curve.

References:

[1] Jewell, J. L., Scherer, A., McCall, S. L., Gossard, A. C. & English, J. H. GaAs-AlAs monolithic microresonator arrays. *Appl. Phys. Lett.* **51**, 94–96 (1987).
[2] Davies, H. The reflection of electromagnetic waves from a rough surface. *Proc. IEE* **101**, 209–214 (1954).
[3] Bennett, H. E. & Porteus, J. O. Relation between surface roughness and specular reflectance at normal incidence. *J. Opt. Soc. Am.* **51**, 123–129 (1961).
[4] Alexandrovski, A., Fejer, M., Markosian, A. & Route, R. Photothermal common-path interferometry (PCI): new developments. In *Proc. SPIE 7193, Solid State Lasers XVIII: Technology and Devices*. **7193D** (2009).
[5] Harry, G., Bodiya, T. & DeSalvo, R. *Optical Coatings and Thermal Noise in Precision Measurement*. (Cambridge University Press, 2012). pp. 45, 136, 161, 295, 299.
[6] Krishnamurthy, S., Yu, Z. G., Gonzalez, L. P., & Guha, S. Temperature and wavelength-dependent two-photon and free-carrier absorption in GaAs, InP, GaInAs, and InAsP. *J. Appl. Phys.* **109**, 033102 (2011).
[7] Kudman, I. & Seidel, T. Absorption edge in degenerate p-type GaAs. *J. Appl. Phys.* **33**, 771–773 (1962).
[8] Spitzer, W. G. & Whelan, J. M. Infrared absorption and electron effective mass in *n*-type gallium arsenide. *Phys. Rev.* **114**, 59–63 (1959).
[9] Knigge, A., Zorn, M., Wenzel, H., Weyers, M. & Trankle, C. High efficiency AlGaInP-based 650 nm vertical-cavity surface-emitting lasers. *Electron. Lett* **37**, 1222–1223 (2001).
[10] Ettenberg, M. & Paff, R. J. Thermal expansion of AlAs. *J. Appl. Phys.* **41**, 3926–3927 (1970).

DOI: 10.1038/NPHOTON.2013.174

[11] Reinhart, F. K. & Logan, R. A. Interface stress of $Al_xGa_{1-x}As$-GaAs layer structures. *J. Appl. Phys.* **44**, 3171–3175 (1973).

[12] van der Ziel, J. P. & Gossard, A. C. Absorption, refractive index, and birefringence of AlAs-GaAs monolayers. *J. Appl. Phys.* **48**, 3018–3023 (1977).

[13] Adachi, S. & Oe, K. Internal strain and photoelastic effects in $Ga_{1-x}Al_xAs$/GaAs and $In_{1-x}Ga_xAs_yP_{1-y}$/InP crystals. *J. Appl. Phys.* **54**, 6620–6627 (1983).

[14] Adachi, S. *Physical Properties of III-V Semiconductor Compounds: InP, InAs, GaAs, GaP, InGaAs, and InGaAsP* (John Wiley & Sons, New York, 1992). Chapter 9.

[15] Babic, D. & Corzine, S. Analytic expressions for the reflection delay, penetration depth, and absorptance of quarter-wave dielectric mirrors. *IEEE J. Quantum Electron.* **28**, 514–524 (1992).

[16] Harry, G. M. *et al.* Thermal noise in interferometric gravitational wave detectors due to dielectric optical coatings. *Classical Quant. Grav.* **19**, 897 (2002).

[17] Numata, K., Kemery, A. & Camp, J. Thermal-noise limit in the frequency stabilization of lasers with rigid cavities. *Phys. Rev. Lett.* **93**, 250602 (2004).

[18] Kessler, T., Legero, T. & Sterr, U. Thermal noise in optical cavities revisited. *J. Opt. Soc. Am. B* **29**, 178–184 (2012).

[19] Cerdonio, M., Conti, L., Heidmann, A. & Pinard, M. Thermoelastic effects at low temperatures and quantum limits in displacement measurements. Phys. Rev. D **63**, 082003 (2001).

[20] Numata, K., Ando, M., Yamamoto, K., Otsuka, S. & Tsubono, K. Wide-band direct measurement of thermal fluctuations in an interferometer. Phys. Rev. Lett. **91**, 260602 (2003).

[21] Braginsky, V. B., Gorodetsky, M. L. & Vyatchanin, S. P. Thermo-refractive noise in gravitational wave antennae. *Phys. Lett. A* **271**, 303–307 (2000).

[22] Evans, M. *et al.* Thermo-optic noise in coated mirrors for high-precision optical measurements. *Phys. Rev. D* **78**, 102003 (2008).

[23] Gorodetsky, M. L. Thermal noises and noise compensation in high-reflection multilayer coating. *Phys. Lett. A* **372**, 6813–6822 (2008).

[24] Dawkins, S. T., McFerran, J. J. & Luiten, A. N. Considerations on the measurement of the stability of oscillators with frequency counters. *IEEE Trans. Ultrason. Ferroelectr. Freq. Control* **54**, 918–925 (2007).

[25] Benko, C. *et al.* Full phase stabilization of a Yb:fiber femtosecond frequency comb via high-bandwidth transducers. *Opt. Lett.* **37**, 2196–2198 (2012).

[26] Wong, N. C. & Hall, J. L. Servo control of amplitude modulation in frequency-modulation spectroscopy: demonstration of shot-noise-limited detection. J. Opt. Soc. Am. B **2**, 1527–1533 (1985).

[27] Li, L., Liu, F., Wang, C. & Chen, L. Measurement and control of residual amplitude modulation in optical phase modulation. Review of Scientific Instruments **83**, 043111 (2012).

[28] Kessler, T. *et al.* A sub-40-mHz-linewidth laser based on a silicon single-crystal optical cavity. *Nature Photonics* **6**, 687–692 (2012).